Electrochimica Acta 388 (2021) 138646

Contents lists available at ScienceDirect

Electrochimica Acta

journal homepage: www.elsevier.com/locate/electacta

Orientation effect of zinc vanadate cathode on zinc ion storage performance

Huili Cao[a,1,*], Chao Peng[b,1], Zhiyong Zheng[a], Zhenyun Lan[c], Qinying Pan[a], Ulla Gro Nielsen[d], Poul Norby[c], Xinxin Xiao[a,*], Susanne Mossin[a,*]

[a] Department of Chemistry, Technical University of Denmark, 2800 Kgs. Lyngby, Denmark
[b] Multiscale Crystal Materials Research Center, Shenzhen Institute of Advanced Technology, Chinese Academy of Sciences, Shenzhen 518055, China
[c] Department of Energy Conversion and Storage, Technical University of Denmark, 2800 Kgs. Lyngby, Denmark
[d] Department of Physics, Chemistry and Pharmacy, University of Southern Denmark, Campusvej 55, 5230 Odense M, Denmark

ARTICLE INFO

Article history:
Received 5 March 2021
Revised 8 May 2021
Accepted 15 May 2021
Available online 21 May 2021

Keywords:
Zinc vanadate
Orientation
Density functional theory
Cathode
Zinc-ion battery

ABSTRACT

Rechargeable aqueous zinc-ion battery (ZIB) is considered as a promising energy storage device due to the low cost, high obtainable output voltage, non-toxicity, and environmental friendliness. To achieve an excellent energy storage performance, morphology engineering of cathode materials for aqueous ZIBs is regarded as an important strategy. The impact of dimension and orientation of the cathode material on the electrochemical performance are, however, less studied. Herein, we compare two types of zinc pyrovanadate ($Zn_3V_2O_7(OH)_2 \cdot 2H_2O$, ZnVO) in nanowires and nanoflakes with the same crystal type but different orientations. ZnVO nanowires expose mostly the (001) plane lattice, in contrast to (020) and (110) lattice for ZnVO flakes. Interestingly, nanowires exhibit an excellent specific discharge capacity of 108 mAh g^{-1} after 700 cycles at 2 A g^{-1}, contributed from Faradic and diffusion-controlled capacity. In contrast, nanoflakes deliver a very poor capacity of 1.5 mAh g^{-1} after 700 cycles at 0.1 A g^{-1} with only diffusion-controlled capacity. Density functional theory (DFT) reveals significantly different Zn^{2+} ion diffusion rates in ZnVO along different orientations.

1. Introduction

The rapid development of electric vehicles and portable electronics poses a great demand for energy storage devices [1–4]. Lithium-ion batteries (LIBs) have excellent energy density and a long battery life. They are used in a wide range of commercial applications [5–7]. Battery safety [8–10], the environmental concerns associated with the use of toxic organic electrolytes, as well as the high cost of the lithium metal and recycling, however, hinder their application and further development in power grid related energy storage [11,12]. Accordingly, aqueous rechargeable multivalent-ion batteries have been put forward. These include ZIBs and aluminium-ion batteries (AIBs) [13]. Aqueous electrolytes possess higher ionic conductivity (10^{-1} - 6 S cm^{-1}) compared to the organic counterparts (10^{-3} - 10^{-2} S cm^{-1}) [14]. Besides, multivalent ions can, in principle, enable a very high specific capacity due to the multiple electrons involved [15]. Among these, the aluminium ion can only be operated in acid solutions (pH < 4) due to precipitation of Al_2O_3 at neutral pH. ZIBs can operate in pH-neutral electrolytes and hold tremendous promise as a cheap and safe alternative for grid-scale energy storage [16].

The metallic zinc anode of ZIBs possesses a relatively low redox potential of -0.762 V *vs.* standard hydrogen electrode and a high theoretical specific capacity of 820 mAh g^{-1}. Currently, the major challenges are related to the cathode materials that host Zn^{2+} [17, 18]. The radius of Zn^{2+} is about 0.75 Å, close to that of lithium ion (0.76 Å), but rises sharply to 4.3 Å in the hydrated form [19]. Two classes of cathode materials, including i) tunnel-type with a tunnel diameter above 3.0 Å and ii) layered-type with a large layer spacing (beyond 4.3 Å), have been developed [20]. Tunnel-type materials suffer from a low reversible capacity and a disappointing cycling performance. This is likely due to the narrow interlayer distance that undergoes a significant structure expansion upon Zn^{2+} insertion [20]. In comparison, layered-type materials with a sufficiently large layer spacing to accommodate Zn^{2+} are promising. Vanadium-based materials, including zinc pyrovanadate ($Zn_3V_2O_7(OH)_2 \cdot 2H_2O$, ZnVO), with integrated molecular water in

* Corresponding authors.
E-mail addresses: hucao@kemi.dtu.dk (H. Cao), xixiao@kemi.dtu.dk (X. Xiao), slmo@kemi.dtu.dk (S. Mossin).
[1] These authors contributed equally to this work

https://doi.org/10.1016/j.electacta.2021.138646

the crystal structure, represent classic layered-type materials and enjoy high electronic and ionic conductivity [21].

Morphology engineering of cathode materials has been regarded as an important strategy for better ZIB. Specifically, Alfaruqi et al. [22] fabricated layer-type δ-MnO_2 nanoflakes, delivering a ZIB capacity of 122 mAh g^{-1} at a current density of 83 mA g^{-1}. Meanwhile, Guo et al. [23] synthesized δ-MnO_2 microspheres with the same crystal phase, exhibiting a similar capacity of 120 mAh g^{-1} at 100 mA g^{-1}. This suggests that the morphology may not be the most governing factor for ZIB capacity. Besides morphology, the crystal orientation has been identified as a key factor affecting battery performance [24]. For example, Lin et al. [25] fabricated spinel $LiNi_{0.5}Mn_{1.5}O_4$ (LNMO) particles exposing different crystal facets including (111), (110), and (100) for the LIB anode materials, showing that LNMO with predominant (111) facets exhibited ultra-long battery life with a capacity retention of 78.1% after 3000 cycles and outperformed the ones with (110) and (100) facets. Guo and co-workers [26] discovered that $Li_4Ti_5O_{12}$ with a high number of (400) planes exhibited excellent stability with 83.6% capacity retention after 500 cycles, ascribed to the facile lithium insertion. In the ZIB community, there are also some investigations on the diffusion pathways in different orientations. [27–30] However, only very few investigations examine the orientation effect on the specific ZIB performance.

In this work, we pursue the influence of the predominant crystal planes and facets in ZIBs by rational design of two types of ZnVO materials. The different materials are fabricated via facile reactions of direct precipitation and microwave-assistant growth, respectively. Both types of ZnVO materials have been characterized by solid-state nuclear magnetic resonance (NMR), X-ray diffraction (XRD) and transmission electron microscopy (TEM), providing conclusive evidence that the materials possess the same crystal phase but have different preferred orientations. When used as the cathode material of ZIBs, the ZnVO material with the highly preferred (001) facet orientation exhibits capacities which are an order of magnitude better than a related material in the same type of crystal phase but dominated with (020) and (110) plane lattices.

2. Experimental

2.1. Chemicals

Zinc acetate dihydrate ($Zn(CH_3COO)_2$•$2H_2O$), ammonium metavanadate (NH_4VO_3), and carbon black were bought from Alfa Aesar. Steel meshes were purchased from Lizhiyuan Co., Ltd, China. Poly(vinylidene fluoride) (PVDF, $(CH_2CF_2)_n$, average MW ~534.000), zinc nitrate hexahydrate ($Zn(NO_3)_2$•$6H_2O$), glycine ($C_2H_5NO_2$), zinc trifluoromethanesulfonate ($Zn(CF_3SO_3)_2$), 1-methyl-2-pyrrolidinone (C_5H_8NO, NMP) and zinc foils (thickness: 0.25 mm) were obtained from Sigma-Aldrich, Denmark.

2.2. Synthesis of 2D $Zn_3(OH)_2(V_2O_7)$·$2H_2O$ nanosheets in flower morphology, ZnVF

In a typical synthesis, 1 mmol NH_4VO_3 and 1.5 mmol $Zn(CH_3COO)_2$•$2H_2O$ were dissolved in 20 and 30 mL Milli-Q water, respectively, to form clear solutions. The two solutions were mixed and stirred for 1 h. The resulting precipitate consisting of 2D $Zn_3(OH)_2(V_2O_7)$·$2H_2O$ nanosheets, were collected by centrifugation and subsequently dried in an oven at 50 °C overnight.

2.3. Synthesis of 1D $Zn_3(OH)_2(V_2O_7)$·$2H_2O$ nanowires, ZnVW

1D $Zn_3(OH)_2(V_2O_7)$·$2H_2O$ nanowires were synthesized by a simple microwave method. First, 1 mmol NH_4VO_3 was dissolved in 10 mL Milli-Q water at 80 °C; 1.5 mmol $Zn(NO_3)_2$•$6H_2O$ and glycine were dissolved in 10 mL Milli-Q water. When the two solutions were clear, they were mixed at room temperature and stirred for 10 min. The aged solution was then sealed in a 20 mL microwave vessel and heated at 100 °C for 6 h. The resulting brown precipitate were centrifuged and washed several times; first with a few mL of Milli-Q water and then with ethanol. The solid was allowed to dry in an oven at 50 °C to obtain the final product.

2.4. Material characterization

XRD patterns were measured by an Image Plate Huber G670 Guinier diffractometer with Cu Kα1 radiation in a transmission mode. Scanning electron microscopy (SEM) images were obtained using an AFEG 250 Analytical ESEM under a high vacuum atmosphere. TEM images were recorded by a FEI Tenai T20 operated at 200 kV equipped with a TVIPS XF416 CCD camera. The specific surface area and pore diameter distributions were studied by the Brunauer-Emmett-Teller (BET) method using a Micromeritics ASAP 2020. The thermogravimetric (TGA) and differential thermal analysis was measured in air with a ramping rate of 5 °C min^{-1} and heating up to 700 °C.

^1H and ^{51}V MAS NMR spectra were recorded at 14.1 T on an Agilent 600 MHz NMR spectrometer using a 3.2 mm HXY MAS NMR probe tuned to ^1H and ^{51}V in double resonance mode. ^{51}V MAS NMR spectra were recorded using a short (0.1 μs, ca 10°) pulse, with 1 s relaxation delay and 833 kHz spectral width. Two or more spinning speeds in the range of 15-20 kHz were used for ^{51}V. Single-pulse (90° excitation pulse) and a rotor synchronized Hahn echo (90°-τ-180°-τ-acquisition, τ = 1 rotor period) were used. ^1H MAS NMR spectra were recorded with 20 kHz spinning speed. The magic-angle was set by minimizing the linewidth of the spinning sidebands in the ^{23}Na MAS NMR spectrum of sodium nitrate. ^{51}V MAS NMR spectra were referenced relative to neat $VOCl_3$ (0 ppm) using vanadium pentoxide as a secondary reference. The ^1H MAS NMR spectra were referenced against water ($\delta(^1H)$ = 4.6 ppm) as a secondary reference.

2.5. Electrochemical measurements

The cathode electrode was fabricated by coating a mixture of active material (70%), carbon black (20%), and poly(vinylidene fluoride) (PVDF, 10%) on a stainless-steel mesh followed by drying in a vacuum oven at 120 °C for 12 h. The loading of the active materials was 1–1.3 mg cm^{-2}. The coin cells are assembled to CR2032 type with the Zn metal foil as the anode, glass microfiber filters as the separator, and 3 M $Zn(CF_3SO_3)_2$ as the electrolyte. Cell performance was tested on a Metrohm Autolab potentiostat. The galvanostatic testing of the cell was evaluated in a voltage range of 0.2-1.8 V at various current densities. Cyclic voltammetry (CV) was measured in the same potential range at various scan rates ranging from 0.1 to 0.8 mV s^{-1} and electrochemical impedance spectroscopy (EIS) was recorded at the open-circuit voltage in a frequency range of 0.1 to 100k Hz.

2.6. Density functional theory (DFT) calculations

Spin-polarized DFT calculations were performed by using the Vienna Ab-Initio Simulation Package (VASP). The Perdew-Burke-Ernzerhof (PBE) functional within the generalized gradient approximation were used in this work [31–33]. We applied the projector-augmented wave method to represent the core electrons [34, 35]. The valence electronic states were expanded in plane-wave basis sets with cutoff energies of 450 eV. For the ion migration, the climbing-image nudged elastic band (CI-NEB) method was employed to search for the transition states with three images inserted between the initial state and the final state [36, 37]. The

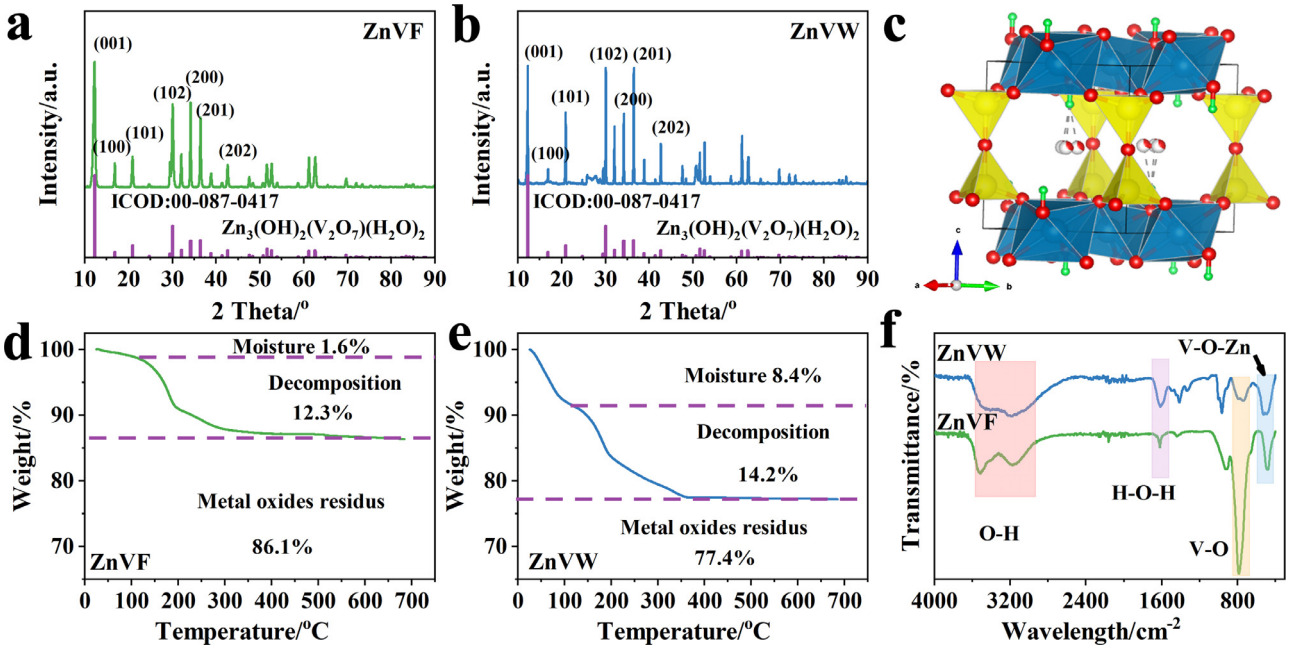

Fig. 1. XRD patterns of ZnVF (a), ZnVW (b) and corresponding crystal structure of ZnVO (c); TGA curves of ZnVF (d) and ZnVW (f); FT-IR spectra of ZnVF and ZnVW (g).

force convergence criterion is 0.05 eV/Å for structural optimization. A k-mesh of (3 × 3 × 2) was used for geometry optimization of ZnVF supercell (a=b=12.10 Å, c=14.39 Å; α=β=90°, γ=120°). The DFT-D3 method was employed to describe dispersion interactions. [38, 39] The GGA+U approach was applied to correct V 3d orbitals with U_{eff} =3.2 eV [40].

3. Results and discussion

3.1. Morphology and structure characterization

The ZnVO materials in this work are fabricated via direct precipitation for flower-shaped nanosheets (ZnVF), and microwave-assisted growth for the nanowires (ZnVW), respectively. The crystalline features were investigated by powder XRD (Fig. 1a,b). The sharp diffraction peaks of the ZnVF (Fig. 1a) suggest good crystallinity, which are well-indexed to the hexagonal ZnVO (ICOD: 01-087-0417). No other crystal phases appear in the XRD patterns, indicating phase-pure materials. Identical peaks are observed for ZnVW (Fig. 1b), confirming the same layer-type crystal structure. The structure consists of ZnO_6 octahedra forming layers with V-O-V columns of the V_2O_7 group in the middle of a sandwich-like structure (Fig. 1c). The crystal water is located between the layers. It is noteworthy that the relative peak intensities are different for ZnVF and ZnVW, revealing that the predominant crystal planes are not the same.

The thermal decomposition processes of both samples were investigated by thermogravimetric analysis (TGA) in air at a ramping rate of 5 °C min^{-1} (Fig. 1d). The weight loss of about 1.6% in the temperature range 30-100 °C is attributed to the evaporation of physically absorbed water. The mass loss of ca. 12.3 % in the range 100-380 °C is assigned to the loss of crystal water and decomposition of hydroxides, along with a phase transition from hexagonal ZnVO to orthorhombic $Zn_3(VO_4)_2$. The same procedure applied to ZnVW reveals an approximately four times higher amount of physically absorbed water on the surface of ZnVW (8.4%, Fig. 1e).

The FTIR spectra of ZnVF and ZnVW (Fig. 1f) confirm the expected stretching and bending modes from the functional groups. The IR band at about 480 cm^{-1} is assigned to symmetric V-O-Zn stretch [41]. The appearance of a peak at about 780 cm^{-1} is due to the V-O-V bonds of corner-sharing VO_4 tetrahedra [42]. The vibration at about 840 cm^{-1} is attributed to the tetrahedral rocking vibration modes of VO_4 [43]. The peaks located at 3000-3600 and 1620 cm^{-1} are assigned to symmetric stretch and bend vibrations of H_2O, respectively [44]. Though the intensities of the bands in the spectra of ZnVF and ZnVW are different, the peak positions are the same. Furthermore, the presence of the peaks confirms that only zinc and vanadium metal oxides are present in the as-prepared samples. It also indicates that the ZnVF and ZnVW share the same local environment of vanadate and are nearly phase pure, but with slightly different amounts of moisture and crystal water.

The ZnVW was dried under vacuum at 200 °C for 2 h before remeasuring the TGA and XRD (Fig. S1a). The weight loss due to loss of moisture and decomposition of the dried ZnVW sample is approximately the same as observed for ZnVF. This weight loss is due to the removal of the physically absorbed water and some of the crystal water. The XRD patterns indicate that the drying process does not change the crystal phase, which remains as hexagonal ZnVO (Fig. S1b).

^{1}H MAS NMR spectroscopy was applied to probe the speciation of hydrogen and vanadium in ZnVF and ZnVW. ^{1}H MAS NMR spectra can be used to confirm the presence of the hydroxide and water molecules inside of the framework, and the physically absorbed surface moisture. Both single-pulse (sp) and Hahn Echo (echo) ^{1}H MAS NMR spectra were recorded on both ZnVF and ZnVW (Fig. S2). The spectra reveal several resonances. It is noted that the crystal structure of ZnVO contains 6 crystallographic inequivalent H, 4 originate from interlayer water and 2 from hydroxide [45]. The obtained spectra were deconvoluted with a minimum number of resonances. ^{1}H MAS NMR spectra of ZnVF and ZnVW are both fitted with 5 resonances. Taking the single pulse ^{1}H MAS NMR spectra as an example, the resonances are at $\delta_{iso}(^1H)$ = 3.7, 5.0, 6.2, 7.3 and 8.2 ppm, where three resonances are from interlayer water, one from physiosorbed water and one from hydroxyl groups bonding to the ZnO_6 octahedron, respectively. The intensity of the resonances has been listed in Table S1. There is a significant difference in the central part of the resonances (around 5 ppm) between the ^{1}H MAS NMR spectra recorded with a single pulse and with a rotor synchronized echo. This intensity loss in the echo experiment

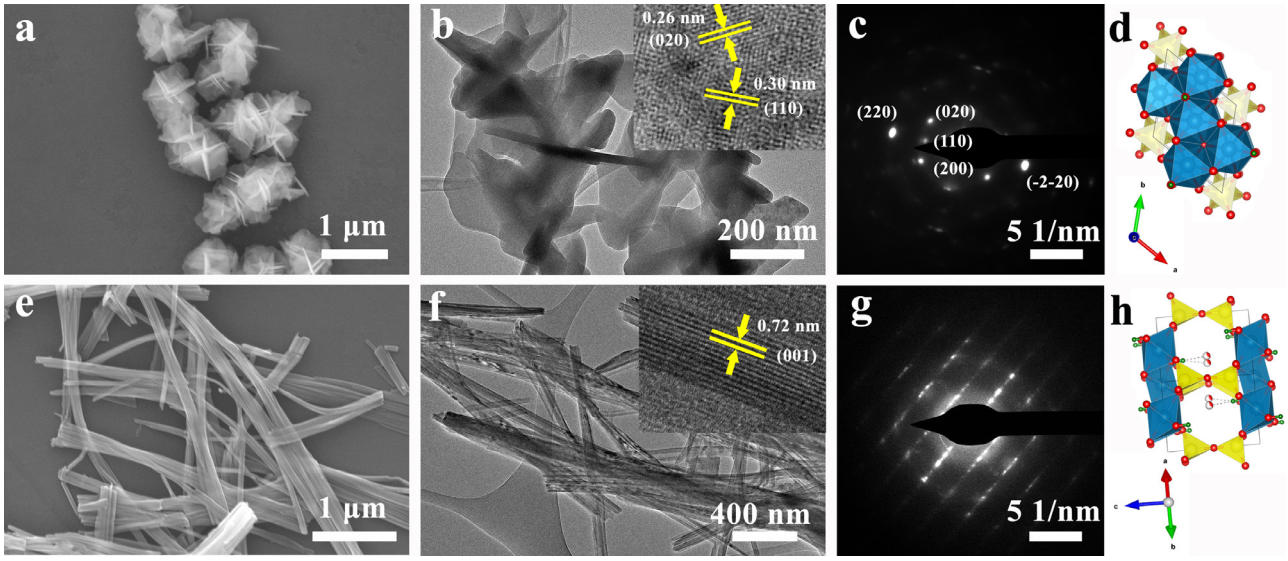

Fig. 2. SEM image, TEM image, SAED, and top-view crystal structure of ZnVF (a-d) and ZnVW (e-h).

is most likely due to the motion of the water molecules on the time scale of the spinning speed (kHz range).

The ^{51}V MAS NMR spectra of both samples contained an intense central transition with a center of gravity at -557.7 ppm and several spinning sidebands from the satellite transitions. The spectrum is characteristic of an orthovanadate influenced by small chemical shift anisotropy and moderate quadrupole interaction [46], as illustrated in Fig. S3. Both ZnVF and ZnVW have a small shoulder at -579.3 ppm of ca 9.4 % intensity as compared to the main resonance. The resonance does not match previously reported values for $Zn_3(VO_4)_2$ (-522 ppm) [47], ZnV_2O_6 (-494 ppm) [48], or $Zn_2V_2O_7$ (-616 ppm) [49] due to the different binding geometries in the various zinc vanadates. This suggests that it is not due to a small impurity of a different zinc vanadate phase in the samples. The presence of the hydroxide bond and the water molecules inside the framework leads to distorted octahedral V-O environments [50]. Thus, according to the ^{51}V MAS NMR analysis, both ZnVF and ZnVW have the same local environment of the vanadate and the samples are nearly phase-pure.

To ascertain the elemental composition, XPS analysis has been conducted for both ZnVF and ZnVW. The XPS survey spectra in Fig. S4 show that both samples are composed of Zn, V, and O. In the Zn 2p spectra, the two obvious peaks at 1022 and 1405 eV correspond to Zn 2p3/2 and Zn 2p1/2 from Zn^{2+}, respectively [51]. The high-resolution V 2p spectra show two strong peaks at 524 and 517 eV from V 2p3/2 and V 2p1/2, indicating that vanadium is in oxidation state +5 in both ZnVF and ZnVW, respectively [52]. Due to the broad peak, a small amount of V^{4+} can be observed as well. The O 1s peak is split into various peaks due to the presence of M-O, O-H, and C-O. [53, 54] The M-O bonds in ZnVO includes both V-O and Zn-O; the C-O is from carbon-containing surface contamination and O-H is from the physically absorbed H_2O, crystal H_2O, and also hydroxide in the structure, corresponding well with the solid state NMR results.

The morphology and orientation of the zinc vanadate products are examined by SEM and TEM. The SEM image indicates that the synthesized ZnVF has a flower-like structure. Each flower with a size of 1 μm is assembled by individual nanoflakes (Fig. 2a). The TEM image shows the detailed nanostructure of the ZnVF (Fig. 2b). The thin flakes are of even thickness and are 200-500 nm in diameter. The lattice fringes can be observed in high-resolution TEM images (inset of Fig. 2b). One lattice fringe with a d spacing of 0.26 nm corresponds to the (020) plane of the ZnVO phase, and the other plane (110) having 30° angles to the (020) plane has a 0.30 nm d spacing, in consistent to the XRD results. Combining the SAED image (Fig. 2c) with the information from high resolution-TEM and XRD, the axis zone of the structures in ZnVF is [001]. A view from the top is shown in Fig. 2d.

In contrast to the dominantly planar structure of ZnVF, ZnVW displays a nanowire structure. The lengths of 1D wires are at micrometer-scale (Fig. 2e). The distribution of nanowires is uniform with diameters of ca. 40 nm. The exposed lattice of the nanowire is the (001) plane lattice, with a d spacing of 0.72 nm (inset of Fig. 2f). The SAED image also confirms the layer structure of ZnVW (Fig. 2g). Fig. 2h shows the orientation of the structure in top-view. The BET surface area analyses of ZnVF and ZnVW were performed by N_2 adsorption-desorption (Fig. S5). It is found that the ZnVW nanowire structure exhibits a much larger specific surface area of 66.6 m^2 g^{-1}, exceeding that of the ZnVF flower structure (15.6 m^2 g^{-1}). The pore size distributions of ZnVF and ZnVW indicate there are no pores on the surface, in agreement with the observations from TEM.

Though the morphologies are different between ZnVF and ZnVW, the formation mechanism obeys the Ostwald ripening process. The variation in preparation temperature leads to different orientations displaying diverse surface energy values and thus various morphologies. Specifically, low temperature (room temperature) leads to zinc vanadate nanoflakes and high temperature (100 °C) leads to nanowires, respectively. In confirmation of this, Fig. S6 shows that the nanowire products can also be fabricated by applying high temperature on the ZnVF material.

3.2. Electrochemical performance

The electrochemical performance of both ZnVF and ZnVW was investigated in coin cells. The cycling performance of ZnVF at 100 mA g^{-1} is shown in Fig. 3a. It delivers a very poor capacity of about 3 mAh g^{-1} in the initial cycle. After 700 cycles, the capacity is maintained at about 1.5 mAh g^{-1}. The electrochemical profile of ZnVF provides evidence on the Zn^{2+} insertion and extraction process during charge and discharge. It is noted that the curves for ZnVF at 100 mA g^{-1} initially shows charge and discharge plateaus at 1.2 and 0.8 V (Fig. 3b), which, however, disappear fast, suggesting poor reversibility of ZnVF. After cycling, the flower morphology is maintained (Fig. 3c and Fig. S7). Furthermore, the high-

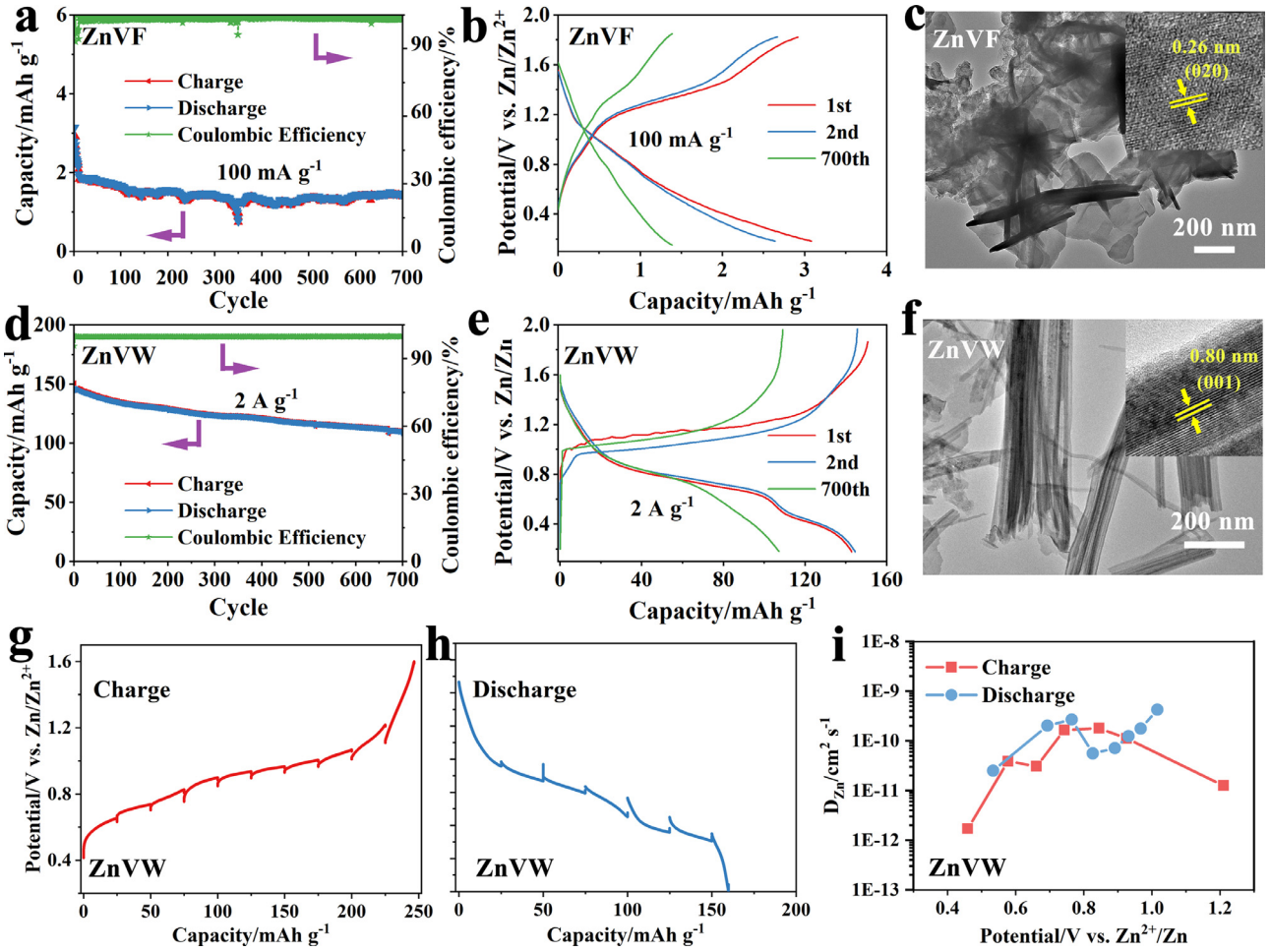

Fig. 3. Charge-discharge cycling profile and coulombic efficiency of cathode electrode (a); galvanostatic discharge/charge curves of the 1st, 2nd, and 700th cycle of ZnVF at the current density of 100 mA g^{-1} (a-b) and ZnVW at a current density of 2A g^{-1} (d-e); TEM images of ZnVF (c) and ZnVW (f) after cycling (insets are high-resolution TEM images). GITT curves and the calculated chemical diffusivity coefficient (D) versus the specific capacity for Zn^{2+} in ZnVW electrode (g-i).

resolution TEM image obtained after cycling show that the interplanar spacing of 0.26 nm for (020) is also maintained.

In contrast, ZnVW initially delivers about 140 mAh g^{-1} at a high current density of 2A g^{-1} (Fig. 3d), about 50 times higher than that of ZnVF. After 700 cycles, the capacity is well retained at 108 mAh g^{-1}, suggesting a high cycling stability. The galvanostatic discharge/charge curves of ZnVW in Fig. 3e show that there are two obvious plateau regions at 1.0/1.2 V, and 0.8/0.5 V, respectively, indicating the storage of more Zn^{2+} ions compared to ZnVF. After 700 cycles, one pair of plateaus (0.8–1.2 V) are still present at the same potentials. The stable structure is further verified by TEM and SEM. Interestingly, the interplanar spacing of the exposed (001) plane spacing increases from the initial value of 0.72 to 0.80 nm. This proves that Zn^{2+} ion has been inserted into the (001) plane lattice, the crystalline phase remaining the same. The XRD patterns in different charge and discharge states show that the crystal phase of the cathode material is maintained. The slight shift of the peak for the (001) plane at high voltage is a further proof of the intercalation in this plane (Fig. S8). Both ZnVF and ZnVW electrode materials are stable when soaking into the electrolyte for several days, see Fig. S9. The large amount of Zn^{2+} ions insertion causes the reduction of vanadium (Fig. S10). The as-fabricated ZnVW material was tested by galvanostatic test (Fig. S11), exhibiting reversible capacities of 227, 198, 166, 118, 86, and 64 mAh g^{-1} at current densities of 100, 200, 400, 800, 1600, and 3200 mA g^{-1}, respectively. Furthermore, the specific Zn^{2+} ion diffusion coefficient value (D) in the active material is calculated from the galvanostatic intermittent titration technique (GITT), see Fig. S12. The analysis is based on the following equation [55]:

$$D = \frac{4L^2}{\pi t}\left(\frac{\Delta E_s}{\Delta E_t}\right)^2 \quad (1)$$

where 'L' is the thickness of the mass loading on steel mesh; 't' denotes the constant current pulse time; 'ΔE_s' is the change of the voltage during a single-step GITT experiment, and 'ΔE_t' is the voltage change during a constant pulse t. It is noted that the average D values at charge and discharge are in the range of 10^{-11}-10^{-10} cm^2 s^{-1} (Fig. 3g–i). These large values, suggesting fast Zn^{2+} ion diffusion during the reactions, are ascribed to the exposed large lattice spaces and the low Faradic electron transfer resistance.

In general, the energy storage mechanism is a combination of Faradic capacitive behavior and diffusion-controlled behavior. CV was performed to distinguish the two types of charge storage mechanisms in both ZnVF and ZnVW. The CV curves of ZnVF were measured in a potential range of 0.2 to 1.8 V (vs. Zn/Zn^{2+}), with minimal hydrogen or oxygen evolution reactions, and at different scan rates ranging from 0.1 to 0.8 mV s^{-1} (Fig. 4a). The CV curves exhibit different peaks at a low scan rate, because the low ion diffusion coefficient leads to an irreversible insertion and extraction of the Zn^{2+} ion in the crystal structure at a high scan rate. ZnVW exhibits two distinct pairs of peaks at around 1.0/0.9 V (peak1/peak2) and 0.75/0.5 V (peak 3/peak 4), assigned to Zn^{2+} intercalation and extraction in a two-step process (Fig. 4c). Based on the previous reports and power law principles, the relationship

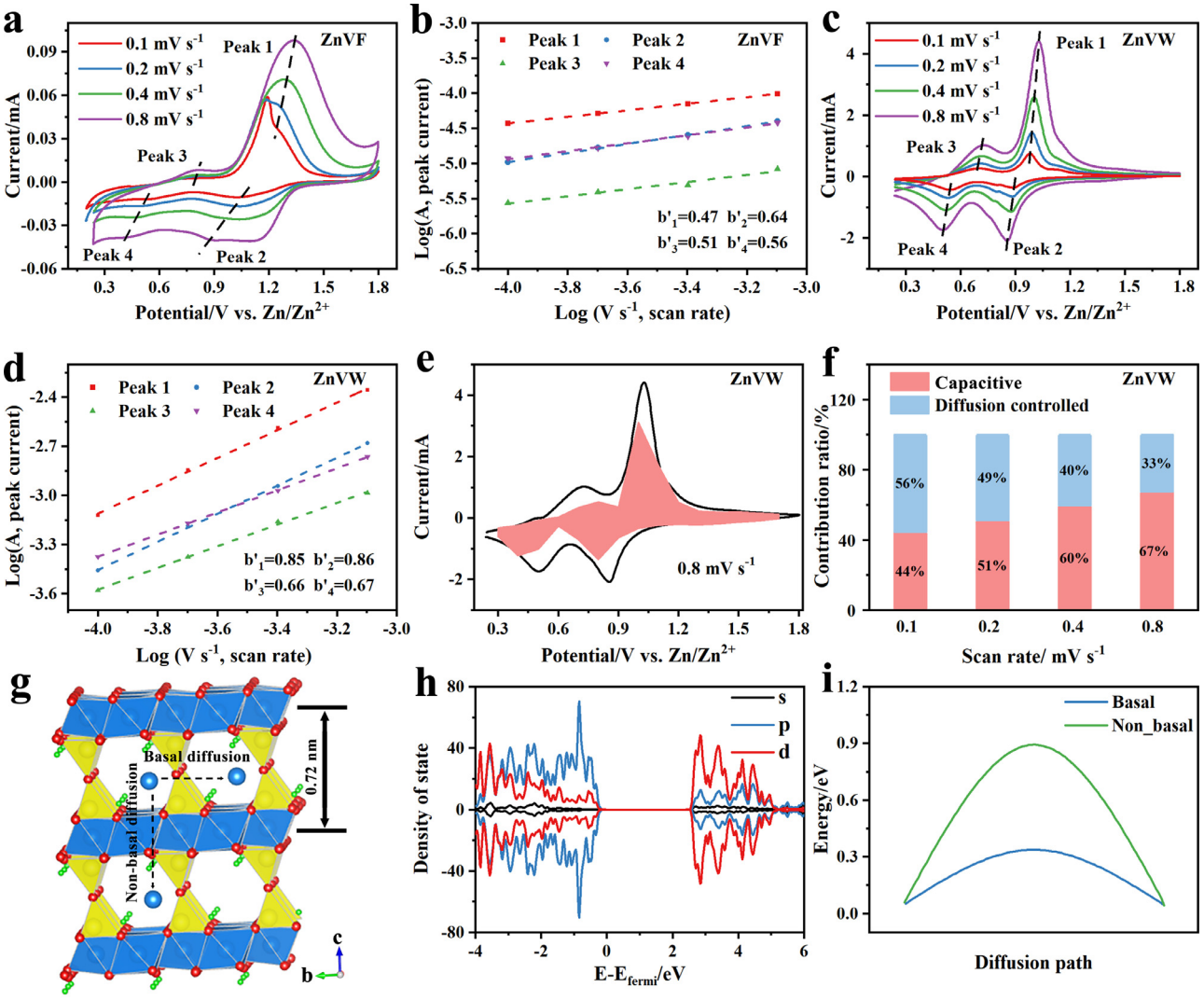

Fig. 4. CV curves and the dependence of the peak currents at various scan rates from 0.1 to 0.8 mV s^{-1} of ZnVF (a, b) and ZnVW (c, d); Capacitive contribution (pink part) and diffusion contribution (void part) at 0.8 mV s^{-1} (e); Normalized contribution ratio of the capacitive capacity at different scan rates (f); The possible diffusion pathways of Zn^{2+} ion in the crystal structures (g); Projected density of state (pDOS) of the $Zn_3V_2O_7(OH)_2$ bulk structure (h) and the corresponding diffusion energy in two directions (i) (For interpretation of the references to color in this figure, the reader is referred to the web version of this article.).

between peak current and scan rate is $i = a'v^{b'}$ (a' and b' are variables), details given in the Supporting Information. [20,56] The b' values of ZnVW are 0.85, 0.86, 0.66, and 0.67 during charging and discharging process, as compared to 0.47, 0.64, 0.51, and 0.56 of ZnVF, indicating complete diffusion-controlled kinetics in ZnVF and a partial capacitive contribution in ZnVW. For example, 67% of the current can be assigned to the capacitive response at 0.8 mV s^{-1} (calculation is given in Supporting Information and Fig. S13), see Fig. 4e. With decreasing scan rate, the diffusion-controlled contribution increases, consistent to previously reported materials undergoing an intercalation mechanism [57,58]".

3.3. DFT calculation

The Zn ion diffusion pathway in the crystal structure is proposed to be the main reason for the significant difference in the capacity of ZnVF and ZnVW. The possible diffusion pathways of Zn^{2+} in the crystal structures in $Zn_3V_2O_7(OH)_2$ are given in Fig. 4g. The projected density of state (pDOS) of the $Zn_3V_2O_7(OH)_2$ bulk structure is shown in Fig. 4h. 2D flakes of ZnVF expose mainly the (001) basal plane, consisting of compact layers of ZnO_6 octahedras (blue colour in Fig. 4g). Zn^{2+} intercalation in that direction has to go through the small lattice spacing between ZnO_6 octahedras with large hindrance. In contrast, ZnVW exposes the (010) non-basal plane (or (001) plane lattice), comprising the ZnO_6 octahedron layers connecting with each other through an oxygen bridge. The much larger interlayer spacing of 0.72 nm is identified between the ZnO_6 layers, allowing facile Zn^{2+} diffusion.

DFT calculations were carried out to investigate the migration barrier of Zn^{2+} though each of those two planes. As shown in Fig. 4i, Zn^{2+} intercalation from the compact layer of ZnO_6 octahedrons in ZnVF is regarded as non-basal diffusion, while Zn^{2+} migration in between the ZnO_6 layers in ZnVW is described as basal diffusion (along the basal plane). The climbing-image nudged elastic band (CI-NEB) calculations shows that the basal diffusion of Zn^{2+} in the ZnVW structure has a much lower energy barrier of 0.31 eV, compared to the non-basal diffusion in the ZnVF of 0.89 eV. We compare the diffusion rates of Zn^{2+} in the two systems further by using transition-state theory which can be expressed as follows [59]:

$$r = ve^{\left(-\frac{E_a}{KT}\right)} \quad (2)$$

where v, E_a, k and T are pre-exponential factor, diffusion barrier, Boltzmann constant (8.617×10^{-5} eV/K) and temperature (298 K),

respectively. Zn^{2+} diffusion in the b direction (non-basal diffusion) is around a factor of 10^9 faster than that in the c direction. It reveals that ZnVO exposing a large enough lattice spacing can easily accommodate the intercalation of Zn^{2+}. In addition, electrochemical impedance spectroscopy (EIS) (Fig. S14) reveals that the electrical resistance of the ZnVW is about 9 times lower than that of ZnVF, leading to a more efficient Zn^{2+} transportation. The Zn^{2+} diffusion coefficient at the dilute limit in ZnVW calculated by DFT at room temperature (300 K) is ca. 5.6×10^{-8} cm^2 s^{-1}, which is higher than the value from GITT (10^{-11}-10^{-10}). It might be due to the ideal crystal structure and short diffusion pathway applied in DFT calculation, differing from the real experiment situation.

4. Conclusions

In conclusion, we have observed that ZnVF and ZnVW, in the same crystal phase and chemical environment, show vastly different performance as ZIB cathode material. Using TEM and ss-NMR, we identify the differences between the as-prepared samples with respect to morphology, dimension, and crystal orientation. When used as the cathode electrode of ZIBs, ZnVW exhibits lower polarization, higher electrochemical activity, higher electrical conductivity, and faster ion diffusion capability than ZnVF. In addition, ZnVW has a combined contribution of diffusion-controlled and Faradic capacitive behavior, leading to the great Zn^{2+} storage performance. The knowledge about the critical requirement for the crystalline orientation is highly valuable for the development of next-generation cathode materials.

Supporting Information: Additional information and figures include TGA curve and XRD pattern of ZnVW dried under vacuum; ^1H and ^{51}V ss-NMR spectra, XPS spectra, N_2 adsorption-desorption isotherms, SEM images, XRD patterns and XPS spectra of the charge and discharge states, EIS spectra of the ZnVF and ZnVW. Rate performance, plots of $v^{-1/2}$ *vs.* $i/v^{-1/2}$ at different potential states of ZnVW.

Declaration of Competing Interest

There are no conflicts to declare.

Credit authorship contribution statement

Huili Cao: Conceptualization, Methodology, Validation, Formal analysis, Investigation, Resources, Data curation, Writing - original draft, Visualization. **Chao Peng:** Conceptualization, Data curation, Validation, Visualization. **Zhiyong Zheng:** Resources, Validation, Formal analysis. **Zhenyun Lan:** Validation, Formal analysis. **Qinying Pan:** Formal analysis, Investigation. **Ulla Gro Nielsen:** Formal analysis, Investigation. **Poul Norby:** Supervision, Writing - review & editing. **Xinxin Xiao:** Formal analysis, Supervision, Writing - review & editing. **Susanne Mossin:** Formal analysis, Supervision, Writing - review & editing, Project administration.

Acknowledgments

This article is dedicated to Professor Jens Ulstrup on the occasion of his 80th birthday. The authors gratefully acknowledge the financial support from the China Scholarship Council for a Ph.D. scholarship (No. 201706220078) to H. C. and a VILLUM Experiment (grant No. 35844) to X. X.. C. P. thanks the Natural Science Foundation of Hunan Province (2019JJ50526). Mr. Christian B. Jørgensen is thanked for assistance with the NMR experiments. U. G. N. acknowledges funding from the Danish Council for Independent Research (DFF-7014-00198). The 600 MHz NMR spectrometer is part of the Villum center for bioanalytical analyses.

Data availability

Raw data from all measurements are available from the authors.

Supplementary materials

Supplementary material associated with this article can be found, in the online version, at doi:10.1016/j.electacta.2021.138646.

References

[1] P. Hu, T. Zhu, X. Wang, X. Wei, M. Yan, J. Li, W. Luo, W. Yang, W. Zhang, L. Zhou, Z. Zhou, L. Mai, Highly durable $Na_2V_6O_{16}$•$1.63H_2O$ nanowire cathode for aqueous zinc-ion battery, Nano Lett. 18 (2018) 1758–1763.
[2] Y. Zhang, Y. An, L. Wu, H. Chen, Z. Li, H. Dou, V. Murugadoss, J. Fan, X. Zhang, X. Mai, Z. Guo, Metal-free energy storage systems: combining batteries with capacitors based on a methylene blue functionalized graphene cathode, J. Mater. Chem. A 7 (2019) 19668–19675.
[3] B. Kirubasankar, V. Murugadoss, J. Lin, T. Ding, M. Dong, H. Liu, J. Zhang, T. Li, N. Wang, Z. Guo, S. Angaiah, *In situ* grown nickel selenide on graphene nanohybrid electrodes for high energy density asymmetric supercapacitors, Nanoscale 10 (2018) 20414–20425.
[4] H. Lyu, P. Li, J. Liu, S. Mahurin, J. Chen, D.K. Hensley, G.M. Veith, Z. Guo, S. Dai, X.-G. Sun, Aromatic polyimide/graphene composite organic cathodes for fast and sustainable lithium-ion batteries, ChemSusChem 11 (2018) 763–772.
[5] Y. Tian, Y. An, C. Wei, B. Xi, S. Xiong, J. Feng, Y. Qian, Flexible and free-standing $Ti_3C_2T_x$ MXene@Zn paper for dendrite-free aqueous zinc metal batteries and nonaqueous lithium metal batteries, ACS Nano 13 (2019) 11676–11685.
[6] X. Lou, C. Lin, Q. Luo, J. Zhao, B. Wang, J. Li, Q. Shao, X. Guo, N. Wang, Z. Guo, Crystal structure modification enhanced $FeNb_{11}O_{29}$ anodes for lithium-ion batteries, ChemElectroChem 4 (2017) 3171–3180.
[7] J. Guan, Y. Li, Y. Guo, R. Su, G. Gao, H. Song, H. Yuan, B. Liang, Z. Guo, Mechanochemical process enhanced cobalt and lithium recycling from wasted lithium-ion batteries, ACS Sustain. Chem. Eng. 5 (2017) 1026–1032.
[8] H. Lyu, C.J. Jafta, I. Popovs, H.M. Meyer, J.A. Hachtel, J. Huang, B.G. Sumpter, S. Dai, X.G. Sun, A dicyanobenzoquinone based cathode material for rechargeable lithium and sodium ion batteries, J. Mater. Chem. A 7 (2019) 17888–17895.
[9] H. Lyu, Y. Li, C.J. Jafta, C.A. Bridges, H.M. Meyer, A. Borisevich, M.P. Paranthaman, S. Dai, X.G. Sun, Bis(trimethylsilyl) 2-fluoromalonate derivatives as electrolyte additives for high voltage lithium ion batteries, J. Power Sources 412 (2019) 527–535.
[10] H. Lyu, J. Liu, S. Qiu, Y. Cao, C. Hu, S. Guo, Z. Guo, Carbon composite spun fibers with in situ formed multicomponent nanoparticles for a lithium-ion battery anode with enhanced performance, J. Mater. Chem. A 4 (2016) 9881–9889.
[11] X. Wang, B. Xi, Z. Feng, W. Chen, H. Li, Y. Jia, J. Feng, Y. Qian, S. Xiong, Layered $(NH_4)_2V_6O_{16}$•$1.5H_2O$ nanobelts as a high-performance cathode for aqueous zinc-ion batteries, J. Mater. Chem. A 7 (2019) 19130–19139.
[12] P. Tan, B. Chen, H. Xu, H. Zhang, W. Cai, M. Ni, M. Liu, Z. Shao, Flexible Zn– and Li–air batteries: recent advances, challenges, and future perspectives, Energy Environ. Sci. 10 (2017) 2056–2080.
[13] L. Fan, Y. Ru, H. Xue, H. Pang, Q. Xu, Vanadium-based materials as positive electrode for aqueous zinc-ion batteries, Adv. Sustain. Syst. 4 (2020) 2000178.
[14] B. Tang, L. Shan, S. Liang, J. Zhou, Issues and opportunities facing aqueous zinc-ion batteries, Energy Environ. Sci. 12 (2019) 3288–3304.
[15] G. Fang, J. Zhou, A. Pan, S. Liang, Recent advances in aqueous zinc-ion batteries, ACS Energy Lett. 3 (2018) 2480–2501.
[16] Y. Zhong, X. Xu, J.P. Veder, Z. Shao, Self-recovery chemistry and cobalt-catalyzed electrochemical deposition of cathode for boosting performance of aqueous zinc-ion batteries, iScience 23 (2020) 100943.
[17] J. Shin, D.S. Choi, H.J. Lee, Y. Jung, J.W. Choi, Hydrated intercalation for high--performance aqueous zinc ion batteries, Adv. Energy Mater. 9 (2019) 1900083.
[18] Z. Wu, C. Lu, Y. Wang, L. Zhang, L. Jiang, W. Tian, C. Cai, Q. Gu, Z. Sun, L. Hu, Ultrathin VSe_2 nanosheets with fast ion diffusion and robust structural stability for rechargeable zinc-ion battery cathode, Small 16 (2020) 2000698.
[19] Y. Tian, G.-D. Li, J.-S. Chen, Chemical formation of mononuclear univalent zinc in a microporous crystalline silicoaluminophosphate, J. Am. Chem. Soc. 125 (2003) 6622–6623.
[20] Y. Yang, Y. Tang, G. Fang, L. Shan, J. Guo, W. Zhang, C. Wang, L. Wang, J. Zhou, S. Liang, Li^+ intercalated V_2O_5•nH_2O with enlarged layer spacing and fast ion diffusion as an aqueous zinc-ion battery cathode, Energy Environ. Sci. 11 (2018) 3157–3162.
[21] Y. Yang, Y. Tang, S. Liang, Z. Wu, G. Fang, X. Cao, C. Wang, T. Lin, A. Pan, J. Zhou, Transition metal ion-preintercalated V_2O_5 as high-performance aqueous zinc-ion battery cathode with broad temperature adaptability, Nano Energy 61 (2019) 617–625.
[22] M.H. Alfaruqi, J. Gim, S. Kim, J. Song, D.T. Pham, J. Jo, Z. Xiu, V. Mathew, J. Kim, A layered δ-MnO_2 nanoflake cathode with high zinc-storage capacities for eco-friendly battery applications, Electrochem. Commun. 60 (2015) 121–125.
[23] C. Guo, Q. Zhou, H. Liu, S. Tian, B. Chen, J. Zhao, J. Li, A case study of β- and δ-MnO_2 with different crystallographic forms on ion-storage in rechargeable aqueous zinc ion battery, Electrochim. Acta 324 (2019) 134867.

[24] T. Chen, Y. Bai, X. Xiao, H. Pang, Exposing (001) crystal facet on the single crystalline β-$Ni(OH)_2$ quasi-nanocubes for aqueous Ni-Zn batteries, Chem. Eng. J. 413 (2021) 127523.
[25] H.B. Lin, Y.M. Zhang, H.B. Rong, S.W. Mai, J.N. Hu, Y.H. Liao, L.D. Xing, M.Q. Xu, X.P. Li, W.S. Li, Crystallographic facet- and size-controllable synthesis of spinel $LiNi_{0.5}Mn_{1.5}O_4$ with excellent cyclic stability as cathode of high voltage lithium ion battery, J. Mater. Chem. A 2 (2014) 11987–11995.
[26] J. Guo, W. Zuo, Y. Cai, S. Chen, S. Zhang, J. Liu, A novel $Li_4Ti_5O_{12}$-based high--performance lithium-ion electrode at elevated temperature, J. Mater. Chem. A 3 (2015) 4938–4944.
[27] M. Song, H. Tan, D. Chao, H.J. Fan, Recent advances in Zn-Ion batteries, Adv. Funct. Mater. 28 (2018) 1802564.
[28] X. Li, L. Ma, Y. Zhao, Q. Yang, D. Wang, Z. Huang, G. Liang, F. Mo, Z. Liu, C. Zhi, Hydrated hybrid vanadium oxide nanowires as the superior cathode for aqueous Zn battery, Mater. Today Energy 14 (2019) 100361.
[29] D. Chen, M. Lu, B. Wang, H. Cheng, H. Yang, D. Cai, W. Han, H.J. Fan, High-mass loading V_3O_7•H_2O nanoarray for Zn-ion battery: new synthesis and two-stage ion intercalation chemistry, Nano Energy 83 (2021) 105835.
[30] Y. Liu, P. Hu, H. Liu, X. Wu, C. Zhi, Tetragonal VO_2 hollow nanospheres as robust cathode material for aqueous zinc ion batteries, Mater. Today Energy 17 (2020) 100431.
[31] J.P. Perdew, K. Burke, M. Ernzerhof, Generalized gradient approximation made simple, Phys. Rev. Lett. 77 (1996) 3865–3868.
[32] G. Kresse, J. Furthmüller, Efficiency of ab-initio total energy calculations for metals and semiconductors using a plane-wave basis set, Comput. Mater. Sci. 6 (1996) 15–50.
[33] G. Kresse, J. Hafner, Ab initio molecular-dynamics simulation of the liquid-metal–amorphous-semiconductor transition in germanium, Phys. Rev. B 49 (1994) 14251–14269.
[34] G. Kresse, D. Joubert, From ultrasoft pseudopotentials to the projector augmented-wave method, Phys. Rev. B 59 (1999) 1758–1775.
[35] P.E. Blöchl, O. Jepsen, O.K. Andersen, Improved tetrahedron method for brillouin-zone integrations, Phys. Rev. B 49 (1994) 16223–16233.
[36] G. Henkelman, H. Jónsson, Improved tangent estimate in the nudged elastic band method for finding minimum energy paths and saddle points, J. Chem. Phys. 113 (2000) 9978–9985.
[37] G. Henkelman, B.P. Uberuaga, H. Jónsson, A climbing image nudged elastic band method for finding saddle points and minimum energy paths, J. Chem. Phys. 113 (2000) 9901–9904.
[38] S. Grimme, S. Ehrlich, L. Goerigk, Effect of the damping function in dispersion corrected density functional theory, J. Comput. Chem. 32 (2011) 1456–1465.
[39] S. Grimme, J. Antony, S. Ehrlich, H. Krieg, A consistent and accurate ab initio parametrization of density functional dispersion correction (DFT-D) for the 94 elements H-Pu, J. Chem. Phys. 132 (2010) 154104.
[40] L. Ma, N. Li, C. Long, B. Dong, D. Fang, Z. Liu, Y. Zhao, X. Li, J. Fan, S. Chen, Achieving both high voltage and high capacity in aqueous zinc-ion battery for record high energy density, Adv. Funct. Mater. 29 (2019) 1906142.
[41] M.M. Sajid, N.A. Shad, S.B. Khan, Z. Zhang, N. Amin, Facile synthesis of zinc vanadate $Zn_3(VO_4)_2$ for highly efficient visible light assisted photocatalytic activity, J. Alloy. Compd. 775 (2019) 281–289.
[42] S.A. Mahmoud, S.H. Bendary, A.A. Salem, O.A. Fouad, Facile synthesis of high yield two dimensional zinc vanadate nanoflakes, SN Appl. Sci. 1 (2019) 497.
[43] S. Ezhil Arasi, P. Devendran, R. Ranjithkumar, S. Arunpandiyan, A. Arivarasan, Electrochemical property analysis of zinc vanadate nanostructure for efficient supercapacitors, Mater. Sci. Semicond. Process. 106 (2020) 104785.
[44] Y.E. Bhoge, V.J. Patil, T.D. Deshpande, R.D. Kulkarni, Synthesis and anticorrosive performance evaluation of zinc vanadate pigment, Vacuum 145 (2017) 290–294.
[45] N.D. Jensen, N.T. Duong, R. Bolanz, Y. Nishiyama, C.A. Rasmussen, J. Gottlicher, R. Steininger, V. Prevot, U.G. Nielsen, Synthesis and structural characterization of a pure $ZnAl_4(OH)_{12}(SO_4)$•$2.6H_2O$ layered double hydroxide, Inorg. Chem. 58 (2019) 6114–6122.
[46] U.G. Nielsen, A. Boisen, M. Brorson, C.J.H. Jacobsen, H.J. Jakobsen, J. Skibsted, Aluminum orthovanadate ($AlVO_4$): synthesis and characterization by ^{27}Al and ^{51}V MAS and MQMAS NMR spectroscopy, Inorg. Chem. 41 (2002) 6432–6439.
[47] J. Skibsted, C.J.H. Jacobsen, H.J. Jakobsen, ^{51}V Chemical shielding and quadrupole coupling in ortho- and metavanadates from ^{51}V MAS NMR spectroscopy, Inorg. Chem. 37 (1998) 3083–3092.
[48] U.G. Nielsen, H.J. Jakobsen, J. Skibsted, Characterization of divalent metal metavanadates by ^{51}V magic-angle spinning NMR spectroscopy of the central and satellite transitions, Inorg. Chem. 39 (2000) 2135–2145.
[49] U.G. Nielsen, H.J. Jakobsen, J. Skibsted, ^{51}V MAS NMR investigation of ^{51}V quadrupole coupling and chemical shift anisotropy in divalent metal pyrovanadates, J. Phys. Chem. B 105 (2001) 420–429.
[50] N.R. Jaegers, C. Wan, M.Y. Hu, M. Vasiliu, D.A. Dixon, E. Walter, I.E. Wachs, Y. Wang, J.Z. Hu, Investigation of silica-supported vanadium oxide catalysts by High-field ^{51}V magic-angle spinning NMR, J. Phys. Chem. C 121 (2017) 6246–6254.
[51] Y. Zhu, Y. Zhong, G. Chen, X. Deng, R. Cai, L. Li, Z. Shao, A hierarchical $Zn_2Mo_3O_8$ nanodots–porous carbon composite as a superior anode for lithium-ion batteries, Chem. Commun. 52 (2016) 9402–9405 (Cambridge, U. K.).
[52] X. Chen, B. Zhao, Y. Cai, M.O. Tadé, Z. Shao, Amorphous V-O-C composite nanofibers electrospun from solution precursors as binder- and conductive additive-free electrodes for supercapacitors with outstanding performance, Nanoscale 5 (2013) 12589–12597.
[53] H. Lyu, J. Li, T. Wang, B.P. Thapaliya, S. Men, C.J. Jafta, R. Tao, X.-G. Sun, S. Dai, Carbon coated porous titanium niobium oxides as anode materials of lithium-ion batteries for extreme fast charge applications, ACS Appl. Energy Mater. 3 (2020) 5657–5665.
[54] J.L. Qin, H.L. Zhu, N. Lun, Y.X. Qi, Y.J. Bai, $Li_2ZnTi_3O_8$/C anode with high initial coulombic efficiency, long cyclic life and outstanding rate properties enabled by fulvic acid, Carbon 163 (2020) 297–307.
[55] W. Shi, B. Yin, Y. Yang, M.B. Sullivan, J. Wang, Y.-W. Zhang, Z.G. Yu, W.S.V. Lee, J. Xue, Unravelling V_6O_{13} diffusion pathways via CO_2 modification for high-performance zinc ion battery cathode, ACS Nano (2021).
[56] V. Augustyn, J. Come, M.A. Lowe, J.W. Kim, P.-L. Taberna, S.H. Tolbert, H.D. Abruña, P. Simon, B. Dunn, High-rate electrochemical energy storage through Li^+ intercalation pseudocapacitance, Nat. Mater. 12 (2013) 518–522.
[57] L. Jiang, Z. Wu, Y. Wang, W. Tian, Z. Yi, C. Cai, Y. Jiang, L. Hu, Ultrafast zinc-ion diffusion ability observed in 6.0-nanometer spinel nanodots, ACS Nano 13 (2019) 10376–10385.
[58] Z. Wu, Y. Wang, L. Zhang, L. Jiang, W. Tian, C. Cai, J. Price, Q. Gu, L. Hu, A layered $Zn_{0.4}VOPO_4$•$0.8H_2O$ cathode for robust and stable Zn ion storage, ACS Appl. Energy Mater. 3 (2020) 3919–3927.
[59] M.H. Dahan, A. Baranovskiy, Y. Natanzon, Y. Amouyal, A first-principles study of the temperature-dependent diffusion coefficients of silver in the thermoelectric compound PbTe, Acta Mater. 202 (2021) 243–254.